Raman-active modes of $1T'$-WTe$_2$ under tensile strain: A first-principles prediction

Wei Yang,[1,*] Zi-Yang Yuan,[1] Ying-Qi Luo,[1] Yu Yang,[2] Fa-Wei Zheng,[2] Zong-Hai Hu,[1] Xiao-Hui Wang,[1] Yuan-An Liu,[1] and Ping Zhang[2,3,†]

[1]*Beijing Key Laboratory of Work Safety Intelligent Monitoring, Beijing University of Posts and Telecommunications, Beijing 100876, People's Republic of China*
[2]*Institute of Applied Physics and Computational Mathematics, Beijing 100088, People's Republic of China*
[3]*Beijing Computational Science Research Center, Beijing 100084, People's Republic of China*

Monolayer $1T'$-WTe$_2$ attracts rapidly growing interests aiming for promising applications in spintronics, dissipationless transport, and quantum computations. Due to one-dimensional W-W chains, $1T'$-WTe$_2$ exhibits unique anisotropic structure and promising properties, which can be modified by simply applying strains. Based on first-principles calculations, we systematically study the phonon dispersion curves as well as the Raman-active modes of $1T'$-WTe$_2$ under different tensile strains. We find that one branch of acoustic phonon softens at special q points under a critical strain of $\varepsilon_a = 11.55\%$ along the a axis (with W-W chains) direction, or $\varepsilon_b = 7.0\%$ along the b-axis direction and $\varepsilon_{ab} = 8.44\%$ along the biaxial direction. Before reaching such critical strains, the Raman frequencies of A_g^1, A_g^3, and A_g^4 modes, contributing to the main peaks in Raman spectra of $1T'$-WTe$_2$, show anisotropic responses to different strains. The response to biaxial strains is found to be the most sensitive. We find that the frequency shift of A_g^3 mode shows parabolic characters of strained $1T'$-WTe$_2$, then we split it into two parts and it shows a Raman-shift transition at ∼5% strains. While for the A_g^1 and A_g^4 modes, the frequencies change linearly.

I. INTRODUCTION

Among the transition metal dichalcogenides (TMDs) monolayers, a widely concerned two-dimensional material family [1], monolayer $1T'$-WTe$_2$ is a large-gap quantum spin Hall (QSH) insulator [2–11] and shows unconventional spin-torque [12] and gate-tunable superconductivity [13]. As a result, it attracts rapidly growing interests, aiming for promising applications in spintronics, dissipationless transport, and quantum computations. Among $1T'$-TMDs—MX_2 with $M = $ (W, Mo) and $X = $ (Te, Se, S)—theoretically predicted to be a new class of QSH insulators [2], WTe$_2$ is the only one with the $1T'$ phase as the ground state [2] and can be observed under ambient conditions [1,14]. $1T'$-WTe$_2$ with a distorted orthorhombic crystal structure is distinct anisotropy in contrast to the other monolayer TMDs crystallized in 1H (trigonal prismatic coordination) or $1T$ (octahedral coordination) structures. In plane, the covalently bonded W atoms form a zigzag W-W chain, which makes WTe$_2$ structurally one-dimensional and electronically a semimetal [15]. When cutting $1T'$-WTe$_2$ into nanoribbons perpendicular to the W-W chains in our previous study [16], the electronic band opens a gap, and semimetal transforms to semiconductor. Other theoretical studies also found that only 1% tensile strain along the W-W chains can lead to a semimetal to semiconductor or QSH insulator transition [17,18]. Moreover, the Poisson

ration, the in-plane stiffness, and the absorption spectrum of monolayer $1T'$-WTe$_2$ are strongly dependent on and tunable by tensile strain [17].

Strain engineering in different orientations can lead to anisotropic modifications to the structure and properties of two-dimensional materials, which could play important roles in the application of flexible logic devices [19]. Theoretical and experimental studies on graphene [20,21], monolayer h-BN [22,23], and 1H-MX_2 with $M = $ (W, Mo) and $X = $ (Se, S) [24–29] have found that the phonon modes are significantly affected by external strains, and their response can be probed by Raman spectroscopy [30]. In contrast to these 1H structures with in-plane isotropic, $1T'$-WTe$_2$ under strain would exhibit more interesting anisotropic properties. The Raman spectrum of WTe$_2$, from monolayer, few-layer, to bulk as well as alloys [31–40], has been studied to detect the crystal structure, lattice vibration, number of layers, and in-plane anisotropy, however, the Raman spectrum of strained WTe$_2$ has not yet been studied by either theory or experiment.

Based on the first-principles calculations, we provide a thorough study on the changes of crystal structures, phonon dispersion curves, Raman-active modes, and frequencies of monolayer $1T'$-WTe$_2$ under uniaxial (parallel or perpendicular to the W-W chains, respectively) and equibiaxial tensile strains. Here, we only focus on $1T'$-WTe$_2$ under tension since a $1T'$-1H phase transition will occur under compression [41], which may be experimentally challenging to achieve without incurring any buckling response. Through our phonon dispersion calculations, we find that the acoustic branches of phonon are the most sensitive to tensile strains. A soft mode

*Corresponding author: yangwei@bupt.edu.cn
†Corresponding author: zhang_ping@iapcm.ac.cn

with negative frequency occurs at a different q point under different critical strain along the a axis, the b axis, and the ab-biaxial direction, which indicates the structural instability and signifies the ideal strength of $1T'$-WTe$_2$ before rupture. Besides, we also find that Raman-active modes of $1T'$-WTe$_2$ exhibit rich behaviors under external strains, and their corresponding frequency changes are anisotropic. These results indicate that Raman measurements are sufficient to detect the strain magnitudes and structural stability of $1T'$-WTe$_2$.

II. COMPUTATIONAL METHOD

Our calculations are based on density functional theory (DFT) and density functional perturbation theory (DFPT) in pseudopotential plane-wave formalism, as implemented in the QUANTUM ESPRESSO package [42]. The atomic positions and lattice constants for $1T'$-WTe$_2$ are optimized by using the Perdew-Burke-Ernzerhof (PBE) [43] functional, and the cutoff energy of 40 Ry and 400 Ry ($1Ry \approx 13.6$ eV) for the wave functions and the charge density, respectively. A vacuum spacing ~ 13Å is used to prevent the interaction between the WTe$_2$ monolayers. A set of $24 \times 12 \times 1$ k-point sampling is used for Brillouin zone (BZ) integration over electronic states, and a set of $8 \times 4 \times 1$ q-point grid is used to obtain dynamical matrices for phonon calculations. When Fourier transforming the dynamical matrices, one can obtain the interatomic force constant in real space, from which phonon modes and frequencies can be produced. The self-consistent solution of the Kohn-Sham equations is obtained when the total energy changed by less than 10^{-8} Ry and the Hellmann-Feynman force on each atom is less than 10^{-6} Ry/bohr (1 bohr $\approx$ 0.529177 Å). The lattice constants thus are determined with
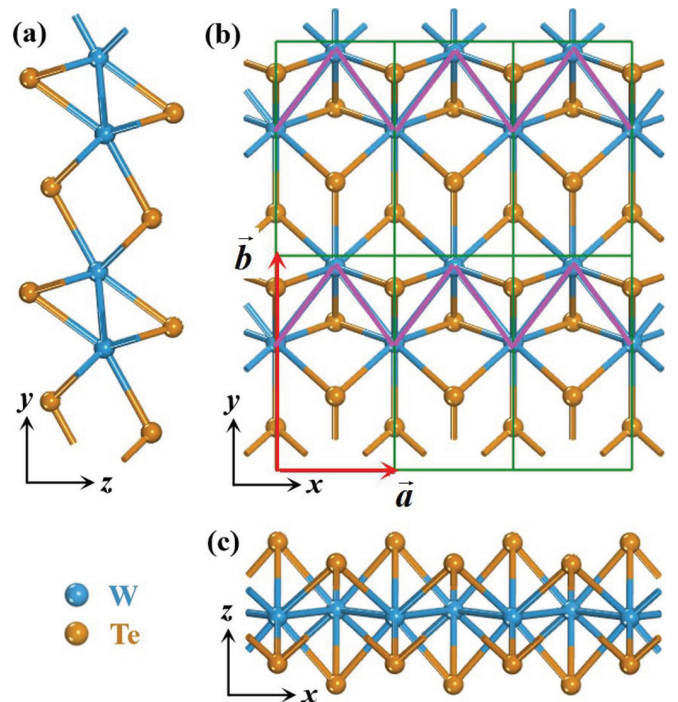

FIG. 1. Crystalline structure of monolayer $1T'$-WTe$_2$ with (a) side view, (b) top view, and (c) front view. The distorted W atoms form one-dimensional zigzag chains indicated by the pink lines. The primitive cells (green rectangles) and the primitive vectors a and b (red arrows) used in the calculations are shown in (b).

$a_0 = 3.49$ Å and $b_0 = 6.31$ Å and agree with the experimental [14,44] and theoretical [13,17] values.
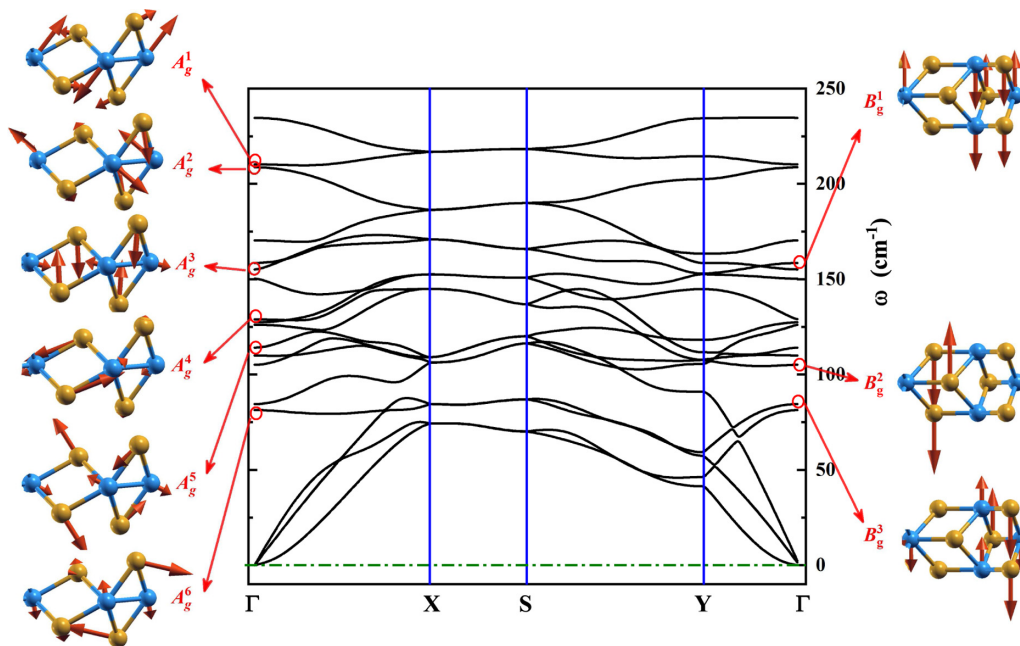

FIG. 2. Calculated phonon dispersion relations and atomic vibration displacements with their corresponding irreducible representations for nine typical Raman-active modes (marked by the red circles at Γ) in monolayer $1T'$-WTe$_2$. Six A_g modes with atoms vibrating in the bc plane are listed in the left panel, and three B_g modes with atoms vibrating in ab plane are listed in the right panel. The q point labels Γ, X, S, Y correspond to $(0,0)$, $(1/2,0)$, $(1/2,1/2)$, $(0,1/2)$, respectively, in a fraction of the reciprocal lattice vectors.

TABLE I. The phonon frequencies of nine Raman-active modes at the Γ point for $1T'$-WTe$_2$ from Raman experiments and first-principles calculations. The unit of frequency has been converted to cm^{-1} for direct comparison with the Raman measurements.

Symmetry	Exp. [31]	Exp. [32]	Exp. [33]	Exp. [34]	Exp. [35]	Cal. [31]	Cal. [32]	Cal. [35]	Cal. [45]	Cal. (This work)
A_g^1	213.2	217	212	216		222.6	219	221.9	208.9	210.3
A_g^2					216.1	220.3		220.5	208.4	208.7
B_g^1						185.7		173.7	161.3	158.5
A_g^3	161.9	164	165	164	164.3	164.5	168	165.9	156.5	155.1
A_g^4	132.8				135.9	137.2	135	136.9	129.9	128.9
A_g^5					119.7	118.5	119	119.7	114.4	114.1
B_g^2					109.4	108.5		110.4	105.8	105.1
B_g^3				86	88.9	93.2	89	92.5	87.2	84.5
A_g^6		81			85.7	81.4		84.6	80.0	81.4

III. RESULTS AND DISCUSSION

The primitive cell of $1T'$-WTe$_2$ is indicated by green rectangle, and its primitive vectors, $\overrightarrow{a}$ and $\overrightarrow{b}$, are indicted by red arrows as shown in Fig. 1(b). Along the a-axis direction, the distorted W atoms form 1D zigzag chains indicated by the pink lines. In the W-W chains as show in Fig. 1(c), the stress (corresponding to $E_{bb} = 110.14 N/m$) is larger than one in the b axis as shown in Fig. 1(a), based on our calculation of Young's modulus matrix

$$E = \begin{pmatrix} 78.59 & 27.68 \\ 28.43 & 110.14 \end{pmatrix} N/m.$$

which are in agreement with previous theoretical [18] and experimental [34] values. Due to the stronger bond strength in W-W chains, one can expect that $1T'$-WTe$_2$ could withstand larger strain along the a-axis direction compared to the b-axis direction. These two directions are the subject of our study. A state of uniaxial strain along the a axis and b axis is constructed by applying the nominal strain and, respectively, where a and b are the strained lattice constants of $1T'$-WTe$_2$.

To obtain Raman-active modes and frequencies of strained $1T'$-WTe$_2$, we first calculate the phonon dispersion curves of the intrinsic one and then analyze the characteristics of Raman-active modes based on group theory. As shown in Fig. 2, there exist 18 phonon branches (three acoustic and

12 optical branches) with six atoms (two tungsten and four tellurium) in the primitive cell of $1T'$-WTe$_2$. Because monolayer WTe$_2$ belongs to the No. 11 space group $P21/m$ and the point group C_{2h}^2, the irreducible representation of the normal modes at Γ point is $6A_g + 3A_u + 3B_g + 6B_u$, in which only nine modes are Raman active among 18 phonon modes based on the symmetry analysis of calculated atomic displacements. These nine Raman-active modes as shown in Fig. 2 are $6A_g + 3B_g$, whose frequencies are shown in Table I with previous theoretical [31,32,35,45] and experimental counterparts [31–35]. Typical Raman spectrum of $1T'$-WTe$_2$ exhibits three prominent Raman peaks at ∼210 cm^{-1}, 160 cm^{-1}, and 130 cm^{-1} denoted as A_g^1, A_g^3, and A_g^4, respectively. Later, we pay special attention to these three Raman-active modes.

Owing to strongly anisotropic mechanical properties of $1T'$-WTe$_2$, we expect that the three Raman-active modes exhibit diverse characteristics for WTe$_2$ under different-direction tensions. Therefore, we then calculate the phonon dispersion relations of strained monolayer WTe$_2$ along a-axis, b-axis, as well as ab-biaxial directions, respectively. Interestingly, as red curves show in Fig. 3, the phonon branches become soft and their frequencies become negative at special q points under different critical strains. For example, when the tensile strain along the a-axis direction approaches 11.55% ($\varepsilon_a = 11.55\%$), one of the acoustic modes of $1T'$-WTe$_2$ becomes imaginary near the S point indicating structural
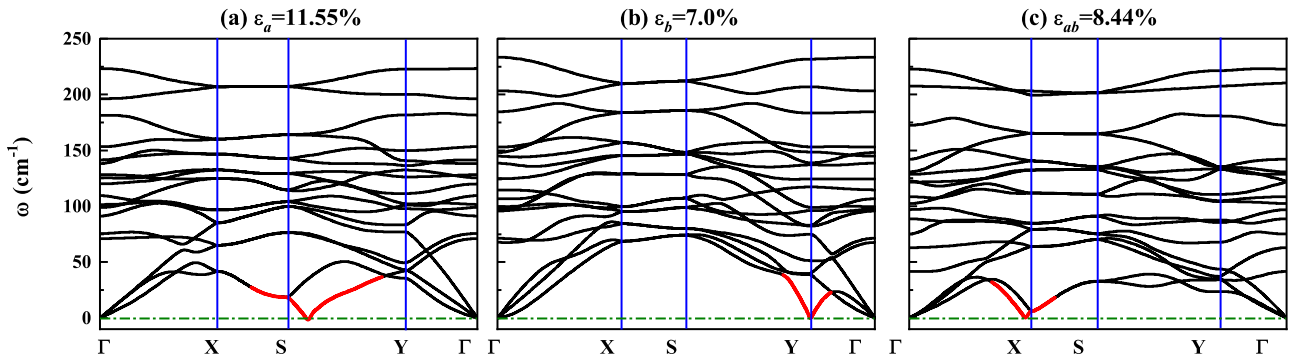

FIG. 3. Calculated phonon dispersion relations for monolayer $1T'$-WTe$_2$ at different critical strains (a) $\varepsilon_a = 11.55\%$ and (b) $\varepsilon_b = 7.0\%$ uniaxial tension along the a and b directions, respectively, and (c) $\varepsilon_{ab} = 8.44\%$ equibiaxial tension. The red phonon dispersion curves show negative-frequency modes (named soft modes) at special q points, indicating the structural instability.

instability, which consists with Torum's (∼11%) [17] and Xiang's (∼12.5%) [18] phonon spectra. In particular, applying strains along the *b*-axis direction, Torun *et al.* [17] found that the strain-stress curve reaches a maximum at the critical strain of 15% (but without supporting phonon dispersion curves), and Xiang *et al.* [18] found that a phonon branch becomes unstable near the Γ point (not pronounced) at the critical strain $\varepsilon_b = 12\%$. But our study of tensile strain along the *b*-axis direction shows that the ideal strength of monolayer $1T'$-WTe$_2$ is 7% with the soft mode occurring at *Y* point exactly, which is smaller than that of WTe$_2$ along the *a*-axis direction with $\varepsilon_a = 11.55\%$. Such anisotropic phonons might be attributed to the 1D structure formed by the W-W chains. Meanwhile, we also calculate the phonon dispersion curves of $1T'$-WTe$_2$ under uniform biaxial strain, as shown in Fig. 3(c), a soft mode occurs near the *X* point at critical strain $\varepsilon_{ab} = 8.44\%$ indicating a possible phase transition with the $1T'$-WTe$_2$ fracture.

Finally, we analyze the response of Raman-active modes (A_g^1, A_g^3, and A_g^4) on the three direction strains before $1T'$-WTe$_2$ rupture. Due to A_g modes containing double-rotation symmetry-axis operation $C_2(z)$ based on the character table for point group C_{2h}, they belong to tangential shear modes with opposite direction vibrations of W-W or Te-Te pairs. Moreover, the vibration displacements of A_g modes (see Fig. 2) are in the *bc* plane of $1T'$-WTe$_2$, perpendicular to the *a*-axis direction, therefore, one can expect that the effects of *a*-axis strain on the A_g modes would be weaker than that of *b*-axis strain. As a result, A_g^4 mode stays relatively unchanged when $1T'$-WTe$_2$ under uniaxial strain along the *a*-axis direction, with a small slope value of -0.29 cm^{-1}/%, as the red line shown in Fig. 4(c). In order to make the frequency/strain ratio of three modes comparable, we put them in one figure with the same scale of the frequency and strain graduations, respectively. In Fig. 4, we do find that the frequency shifts in three modes with *b*-axis strain are all much larger than that with *a*-axis strain, indicating a clear Raman modes anisotropy. This anisotropic Raman-strain response can facilitate the determination of the crystallographic orientation in $1T'$-WTe$_2$. Moreover, when applying biaxial strain to $1T'$-WTe$_2$, the frequencies of three Raman modes also redshift but exhibit most sensitive to biaxial strain compared to uniaxial strains, with corresponding largest slope values. To explain this, we plot Fig. 5. In Fig. 5, one can find that, although the bond angle of W-W chain is almost unchanged when $1T'$-WTe$_2$ under equibiaxial strain, the W-W bond length, the vertical distances in two pairs of Te atoms (c_1 and c_2, respectively) are all dramatically changed compared to the uniaxial strains. This structure modification under biaxial strain, in turn, leads to a considerable change in the Raman-active modes.

For A_g^1 and A_g^4 modes, their frequencies decrease almost linearly with applied strains as shown in Figs. 4(a) and 4(c), respectively, therefore, the strain in $1T'$-WTe$_2$ can be quantified by A_g^1 or A_g^4 mode in Raman spectra. However, for A_g^3 mode, the frequency shift undergoes a sharp turn at about 5% for both uniaxial and biaxial strains, as shown in Fig. 4(b), for example, the calculated biaxial-strain coefficient for A_g^3 mode is down from -2.22 cm^{-1}/% to -6.03 cm^{-1}/%. This redshift transition might be the result from that the lattice symmetry is maintained before 5% strains and then broken after 5%

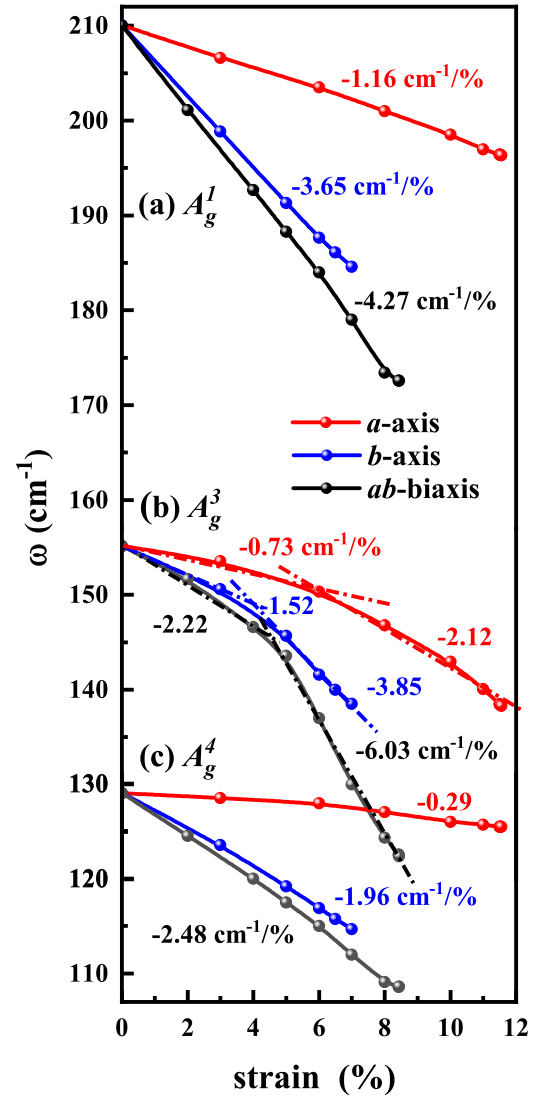

FIG. 4. The phonon frequencies of (a) A_g^1, (b) A_g^3, and (c) A_g^4 modes (corresponding to three Raman peaks experimentally) versus strains along the *a*-axis (red), *b*-axis (blue), and *ab*-biaxis (black) directions, respectively. The solid lines are linear fits to the calculated frequencies (solid symbols) and the corresponding slope values are shown.

strains applied. Because the A_g^3 mode consists of both in-plane and out-of-plane motions as shown in Fig. 2, with regard to the relative motions in pairs of W atoms (in-plane) and pairs of Te atoms (out-of-plane), the parallelogram without W-W chains could maintain its shape, but the parallelogram with W-W chains might be flattened or prolonged. Moreover, the amplitudes of Te atoms are much larger than that of W atoms, especially external strains strengthen the motions of Te atoms but weaken the vibrations of W atoms, which would prompt the symmetry broken at last. So, for this particular A_g^3 transition to external strains and A_g^3 as the most significant peak with the largest intensity in Raman spectra, we hope this phenomena can be tested by future Raman experiments of strained $1T'$-WTe$_2$.
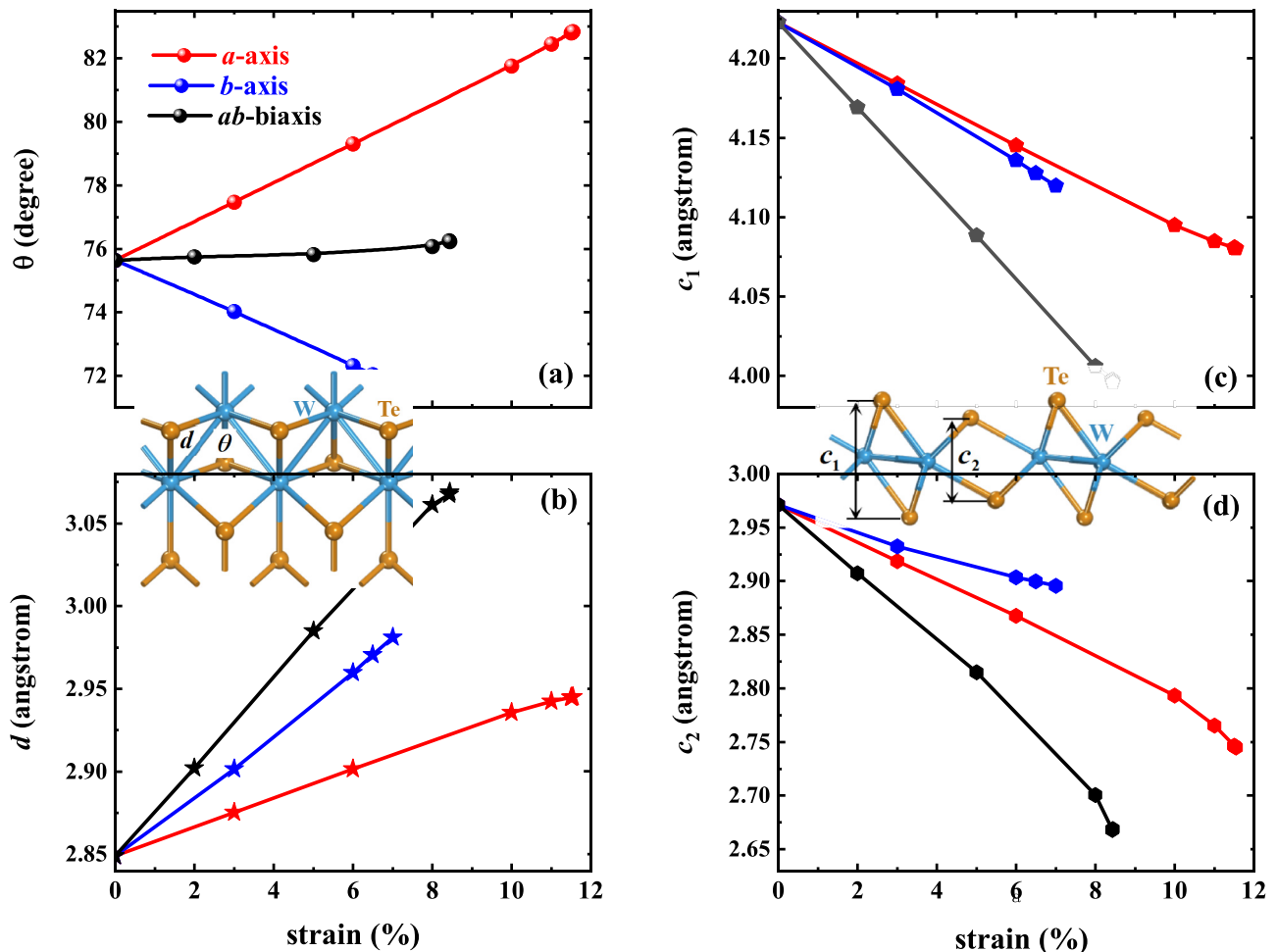
FIG. 5. The calculated (a) W-W-W bond angle θ, (b) W-W bond length d, (c) and (d) vertical distance of two pairs of Te atoms in the c axis, i.e., c_1 and c_2, respectively, as functions of a-axis strain (red lines), b-axis strain (blue lines), and biaxial strain (black lines). The inset crystal configurations are used to depict these calculated variables.

IV. CONCLUSIONS

In conclusion, by using DFT and DFPT simulations, we have systematically obtained the Raman-active modes and frequencies of monolayer 1T'-WTe$_2$ under tensile strains. Our results demonstrate that A_g^1, A_g^3, and A_g^4 modes, corresponding to the main peaks in Raman spectra of 1T'-WTe$_2$, are more sensitive to uniaxial strain along the b-axis direction than that along the a-axis (containing W-W) chains) direction, exhibiting anisotropic Raman-strain response. In particular, biaxial strain induces the largest redshift of the Raman modes compared to the uniaxial strains. Through careful structure configuration analysis, we reveal that the irregularity comes from the dramatic change of the W-W bond length as well as the vertical distances in two pairs of Te atoms under biaxial strain. More interesting, A_g^3 mode undergoes a Raman-shift transition at about 5% for both uniaxial and biaxial strains, different from the A_g^1 and A_g^4 modes whose frequencies show linear dependence on tensile strains. The underlying symmetry reason is revealed to be that the competition and cooperation of the relative motions between W-atom pairs and Te-atom pairs modify the shape of 1T'-WTe$_2$. The revealed Raman modes responses to tensile strain are useful for tracing or detecting operations on 1T'-WTe$_2$ based flexible devices.

[1] J. A. Wilson and A. D. Yoffe, Adv. Phys. **18**, 193 (1969).

[2] X. F. Qian, J. W. Liu, L. Fu, and J. Li, Science **346**, 1344 (2014).

[3] F. P. Zheng, C. Y. Cai, S. F. Ge, X. F. Zhang, X. Liu, H. Lu, Y. D. Zhang, J. Qiu, T. Taniguchi, K. Watanabe, S. Jia, J. S.

Qi, J. H. Chen, D. Sun, and J. Feng, Adv. Mater. **28**, 4845 (2016).

[4] Z.-Y. Jia, Y.-H. Song, X.-B. Li, K. J. Ran, P. C. Lu, H.-J. Zheng, X.-Y. Zhu, Z.-Q. Shi, J. Sun, J. S. Wen, D. Y. Xing, and S.-C. Li, Phys. Rev. B **96**, 041108 (2017).

[5] S. J. Tang, C. F. Zhang, D. Wong, Z. Pedramrazi, H. Z. Tsai, C. J. Jia, B. Moritz, M. Claassen, H. Ryu, S. Kahn, J. Jiang, H. Yan, M. Hashimoto, D. H. Lu, R. G. Moore, C. C. Hwang, C. Hwang, Z. Hussain, Y. L. Chen, M. M. Ugeda, Z. Liu, X. M. Xie, T. P. Devereaux, M. F. Crommie, S. K. Mo, and Z. X. Shen, Nat. Phys. **13**, 683 (2017).

[6] Z. Y. Fei, T. Palomaki, S. F. Wu, W. J. Zhao, X. H. Cai, B. S. Sun, P. Nguyen, J. Finney, X. D. Xu, and D. H. Cobden, Nat. Phys. **13**, 677 (2017).

[7] Y. H. Song, Z. Y. Jia, D. Q. Zhang, X. Y. Zhu, Z. Q. Shi, H. Q. Wang, L. Zhu, Q. Q. Yuan, H. J. Zhang, D. Y. Xing, and S. C. Li, Nat. Commun. **9**, 4071 (2018).

[8] S. Y. Xu, Q. Ma, H. T. Shen, V. Fatemi, S. F. Wu, T. R. Chang, G. Q. Chang, A. M. M. Valdivia, C. K. Chan, Q. D. Gibson, J. D. Zhou, Z. Liu, K. Watanabe, T. Taniguchi, H. Lin, R. J. Cava, L. Fu, N. Gedik, and P. Jarillo-Herrero, Nat. Phys. **14**, 900 (2018).

[9] J. L. Yang, Y. J. Jin, W. P. Xu, B. B. Zheng, R. Wang, and H. Xu, J. Phys. Chem. Lett. **9**, 4783 (2018).

[10] Y. M. Shi, J. Kahn, B. Niu, Z. Y. Fei, B. S. Sun, X. H. Cai, B. A. Francisco, D. Wu, Z.-X. Shen, X. D. Xu, D. H. Cobden and Y.-T. Cui, Sci. Adv. **5**, eaat8799 (2019).

[11] S. F. Wu, V. Fatemi, Q. D. Gibson, K. Watanabe, T. Taniguchi, R. J. Cava, and P. Jarillo-Herrero, Science **359**, 76 (2018).

[12] D. MacNeill, G. M. Stiehl, M. H. D. Guimaraes, R. A. Buhrman, J. Park, and D. C. Ralph, Nat. Phys. **13**, 300 (2017).

[13] S. F. Wu, Bull. Am. Phys. Soc., 2018, https://meetings.aps.org/Meeting/MAR18/Session/B37.4.

[14] B. E. Brown, Acta Crystallogr. **20**, 268 (1966).

[15] M. N. Ali, J. Xiong, S. Flynn, J. Tao, Q. D. Gibson, L. M. Schoop, T. Liang, N. Haldolaarachchige, M. Hirschberger, N. P. Ong, and R. J. Cava, Nature (London) **514**, 205 (2014).

[16] J. H. Wang, W. Yang, M. Zhou, Y. Yang, J. Y. Yan, and P. Zhang, Phys. Lett. A **382**, 2754 (2018).

[17] E. Torun, H. Sahin, S. Cahangirov, A. Rubio, and F. M. Peeters, J. Appl. Phys. **119**, 074307 (2016).

[18] H. Xiang, B. Xu, J. Q. Liu, Y. D. Xia, H. M. Lu, J. Yin, and Z. G. Liu, AIP Adv. **6**, 095005 (2016).

[19] S. K. Deng, A. V. Sumant, and V. Berry, Nano Today **22**, 14 (2018).

[20] C. A. Marianetti and H. G. Yevick, Phys. Rev. Lett. **105**, 245502 (2010).

[21] C. Si, W. H. Duan, Z. Liu, and F. Liu, Phys. Rev. Lett. **109**, 226802 (2012).

[22] W. Yang, Y. Yang, F. W. Zheng, and P. Zhang, Appl. Phys. Lett. **103**, 183106 (2013).

[23] W. Yang, Y. Yang, F. W. Zheng, and P. Zhang, J. Chem. Phys. **139**, 214708 (2013).

[24] S. Horzum, H. Sahin, S. Cahangirov, P. Cudazzo, A. Rubio, T. Serin, and F. M. Peeters, Phys. Rev. B **87**, 125415 (2013).

[25] H. Sahin, S. Tongay, S. Horzum, W. Fan, J. Zhou, J. Li, J. Wu, and F. M. Peeters, Phys. Rev. B **87**, 165409 (2013).

[26] C. R. Zhu, G. Wang, B. L. Liu, X. Marie, X. F. Qiao, X. Zhang, X. X. Wu, H. Fan, P. H. Tan, T. Amand, and B. Urbaszek, Phys. Rev. B **88**, 121301(R) (2013).

[27] C.-H. Chang, X. F. Fan, S.-H. Lin, and J.-L. Kuo, Phys. Rev. B **88**, 195420 (2013).

[28] Y. L. Wang, C. X. Cong, C. Y. Qiu, and T. Yu, Small **9**, 2857 (2013).

[29] Y. L. Wang, C. X. Cong, W. H. Yang, J. Z. Shang, N. Peimyoo, Y. Chen, J. Y. Kang, J. P. Wang, W. Huang, and T. Yu, Nano Res. **8**, 2562 (2015).

[30] X. Zhang, X. F. Qiao, W. Shi, J. B. Wu, D. S. Jiang, and P. H. Tan, Chem. Soc. Rev. **44**, 2757 (2015).

[31] Y. C. Jiang, J. Gao, and L. Wang, Sci. Rep. **6**, 19624 (2016).

[32] Y. Kim, Y. I. Jhon, J. Park, J. H. Kim, S. Lee, and Y. M. Jhon, Nanoscale **8**, 2309 (2016).

[33] Q. J. Song, H. F. Wang, X. L. Xu, X. C. Pan, Y. L. Wang, F. Q. Song, X. G. Wan, and L. Dai, Rsc Adv. **6**, 103830 (2016).

[34] J. Lee, F. Ye, Z. H. Wang, R. Yang, J. Hu, Z. Q. Mao, J. Wei, and P. X. L. Feng, Nanoscale **8**, 7854 (2016).

[35] Y. Cao, N. Sheremetyeva, L. B. Liang, H. Yuan, T. T. Zhong, V. Meunier, and M. H. Pan, 2D Mat. **4**, 035024 (2017).

[36] M. K. Jana, A. Singh, D. J. Late, C. R. Rajamathi, K. Biswas, C. Felser, U. V. Waghmare, and C. N. R. Rao, J. Phys.: Condens. Matter **27**, 285401 (2015).

[37] W. D. Kong, S. F. Wu, P. Richard, C. S. Lian, J. T. Wang, C. L. Yang, Y. G. Shi, and H. Ding, Appl. Phys. Lett. **106**, 081906 (2015).

[38] Q. J. Song, X. C. Pan, H. F. Wang, K. Zhang, Q. H. Tan, P. Li, Y. Wan, Y. L. Wang, X. L. Xu, M. L. Lin, X. G. Wan, F. Q. Song, and L. Dai, Sci. Rep. **6**, 29254 (2016).

[39] X. L. Ma, P. J. Guo, C. J. Yi, Q. H. Yu, A. M. Zhang, J. T. Ji, Y. Tian, F. Jin, Y. Y. Wang, K. Liu, T. L. Xia, Y. G. Shi, and Q. M. Zhang, Phys. Rev. B **94**, 214105 (2016).

[40] S. M. Oliver, R. Beams, S. Krylyuk, I. Kalish, A. K. Singh, A. Bruma, F. Tavazza, J. Joshi, I. R. Stone, S. J. Stranick, A. V. Davydov, and P. M. Vora, 2D Mat. **4**, 045008 (2017).

[41] K. A. N. Duerloo, Y. Li, and E. J. Reed, Nat. Commun. **5**, 4214 (2014).

[42] P. Giannozzi, S. Baroni, N. Bonini, M. Calandra, R. Car, C. Cavazzoni, D. Ceresoli, G. L. Chiarotti, M. Cococcioni, I. Dabo, A. Dal Corso, S. de Gironcoli, S. Fabris, G. Fratesi, R. Gebauer, U. Gerstmann, C. Gougoussis, A. Kokalj, M. Lazzeri, L. Martin-Samos, N. Marzari, F. Mauri, R. Mazzarello, S. Paolini, A. Pasquarello, L. Paulatto, C. Sbraccia, S. Scandolo, G. Sclauzero, A. P. Seitsonen, A. Smogunov, P. Umari, and R. M. Wentzcovitch, J. Phys.: Condens. Matter **21**, 395502 (2009).

[43] J. P. Perdew, K. Burke, and M. Ernzerhof, Phys. Rev. Lett. **77**, 3865 (1996).

[44] C. H. Naylor, W. M. Parkin, Z. L. Gao, H. Kang, M. Noyan, R. B. Wexler, L. Z. Tan, Y. Kim, C. E. Kehayias, F. Streller, Y. R. Zhou, R. Carpick, Z. T. Luo, Y. W. Park, A. M. Rappe, M. Drndic, J. M. Kikkawa, and A. T. C. Johnson, 2D Mat. **4**, 021008 (2017).

[45] J. L. Ma, Y. N. Chen, Z. Han, and W. Li, 2D Mat. **3**, 045010 (2016).